RESEARCH PAPER

Preparation and Characterization of $ZnMn_2O_4$ Nanoparticles to Investigate Its Ability to Produce Reactive Oxygen Species for Application in the Treatment of Cancer by Photodynamic Therapy

Negar Bayati [1], *Ehsan Sadeghi* [1,2] *, *Mostafa Zahedifar* [1,2]

[1] *Department of Physics, University of Kashan, Kashan, Iran*

[2] *Institute of Nano science and nanotechnology, University of Kashan, Kashan, Iran*

ARTICLE INFO

Article History:
Received 10 March 2026
Accepted 15 June 2026
Published 01 July 2026

Keywords:
Nanoparticles
Photodynamic therapy
Photosensitizer
ROS
$ZnMn_2O_4$

ABSTRACT

Photodynamic therapy (PDT) is a photochemistry-based approach that uses the physics of light to activate specific chemicals. In the current study, an attempt is made to synthesize and characterize zinc manganite ($ZnMn_2O_4$) nanoparticles synthesized by co-precipitation method in 1000 °C. Nanoparticles are tiny materials that exist on a scale between 1 and 100 nanometers (nm) in size. At this nanoscale, particles exhibit unique physical, chemical, and biological properties compared to their bulk counterparts. Nanoparticles have been synthesized at sizes comparable to biological molecules such as proteins and DNA. Their reactive oxygen species (ROS) production, magnetic behavior, structural characteristics, textural properties, and photoluminescence were investigated. The lattice parameters of the body-centered tetragonal crystal structure and the size of the nanoparticles range from 12 to 14 nm. $ZnMn_2O_4$ nanoparticles were characterized using X-ray diffraction, field emission scanning electron microscopy, Fourier transform infrared spectroscopy, and UV–visible absorption. The generation of reactive oxygen species (ROS) by these nanoparticles was assessed through the degradation of methylene blue and anthracene, organic pollutants in water and ethanol, under UVC, UVA, and visible light irradiation. Additionally, the magnetic properties of $ZnMn_2O_4$ nanoparticles were investigated using a vibrating sample magnetometer.

How to cite this article
Bayati N., Sadeghi E., Zahedifar M. Preparation and Characterization of $ZnMn_2O_4$ Nanoparticles to Investigate Its Ability to Produce Reactive Oxygen Species for Application in the Treatment of Cancer by Photodynamic Therapy. J Nanostruct, 2026; 16(3):4144-4157. DOI: 10.22052/JNS.2026.03.097

INTRODUCTION

Various treatments have been developed to combat cancer, but only a small proportion have demonstrated significant clinical efficacy. Conventional methods such as chemotherapy, radiotherapy, and surgery are often limited by side effects, resistance, and lack of specificity. In recent years, nanotechnology-based therapies have emerged as promising alternatives due to their ability to enhance targeting and reduce systemic toxicity. Among these, nanoparticle-based photothermal therapy (PTT) and photodynamic therapy (PDT) have shown great potential for cancer treatment. PTT involves the use of

* *Corresponding Author Email: sdgh@kashanu.ac.ir*

This work is licensed under the Creative Commons Attribution 4.0 International License.
To view a copy of this license, visit http://creativecommons.org/licenses/by/4.0/.

nanoparticles that convert light energy into heat to selectively destroy tumor cells, while PDT relies on photosensitizing agents that, upon activation by specific wavelengths of light, generate reactive oxygen species (ROS) to induce cell death.

Photodynamic therapy, in particular, has attracted considerable attention for its minimally invasive nature and dual role in both diagnosis and treatment. It is widely explored for managing tumors, microbial infections, and certain dermatological conditions. The mechanism of PDT is based on a sequence of photochemical and photobiological reactions that ultimately lead to the destruction of malignant tissues, damage to tumor vasculature, and stimulation of the immune response.

Ongoing research focuses on improving the delivery, specificity, and efficiency of photosensitizers through nanoparticle platforms, as well as combining PDT with other treatment modalities such as immunotherapy and chemotherapy for synergistic effects. The scientific basis of photodynamic therapy (PDT) was established in 1900 by Oscar Raab and his professor, Von Tappeiner, who used eosin and sunlight to treat basal cell carcinomas (BCCs). Dougherty reported the first large clinical series of patients successfully treated with PDT about 80 years later [1-4].

The successful delivery of anticancer agents to solid tumors is critical for effective treatment and accurate diagnosis. In the case of engineered nanomaterials, the central principle is that nanoparticles can pass through inter endothelial gaps in tumor blood vessels, which are formed during angiogenesis. These gaps have been found to measure up to 2,000 nm in size. Engineers and scientists use this as a rationale for designing nanoparticles smaller than this threshold, expecting them to passively enter tumors and accumulate in sufficient quantities. Their small size results in a high surface-area-to-volume ratio, which enhances their reactivity and enables unique interactions with biological systems and other materials.

Due to their high surface reactivity, nanoparticles can be engineered for a wide range of specific applications, offering improved material properties such as strength, durability, and conductivity. Such nanomaterials tend to accumulate in tumor regions, where they can convert absorbed near-infrared (NIR) light into heat, generating localized high temperatures that kill cancer cells. Furthermore, many of these materials produce significant levels of reactive oxygen species (ROS), which can also effectively induce cancer cell death [5-9].

Recent advancements in nanomaterials have highlighted the immense potential of multifunctional nanoparticles in medical, environmental, and catalytic applications [10]. Among these, Zn–Mn–O-based nanoparticles stand out due to their exceptional physicochemical properties, biocompatibility, and catalytic efficiency. As ternary oxide materials, Zn–Mn–O nanoparticles offer a synergistic combination of the optical, antibacterial, and redox-active characteristics of zinc and manganese oxides. These properties make them promising candidates for novel therapeutic and environmental applications, particularly in the generation and regulation of reactive oxygen species (ROS) [11].

Reactive oxygen species (ROS) play a dual role in biological and environmental systems. At controlled levels, they act as key mediators in cellular signaling, but when overproduced, they contribute to oxidative stress and cellular damage. The ability of Zn–Mn–O nanoparticles to influence ROS generation holds significant promise for targeted therapeutic strategies, such as cancer treatment via oxidative stress-mediated apoptosis, as well as antimicrobial applications. Furthermore, their catalytic activity—rooted in the redox cycling of Mn and the semiconducting properties of ZnO—makes them valuable for environmental remediation and sensing technologies [12].

Despite their potential, the mechanistic interactions between Zn–Mn–O nanoparticles and ROS dynamics remain underexplored. This paper aims to investigate the synthesis, structural properties, and ROS-modulating capabilities of Zn–Mn–O-based nanoparticles. By systematically evaluating their performance in various biological and catalytic contexts, this study seeks to bridge the gap in understanding the relationship between nanoparticle structure, composition, and ROS activity. These insights are crucial for optimizing Zn–Mn–O nanoparticle design for specific applications in nanomedicine, catalysis, and beyond [13].

$ZnMn_2O_4$ is a mixed-metal oxide compound with the general formula AB_2O_4, where the divalent Zn^{2+} cation occupies the tetrahedral sites and the trivalent Mn^{3+} cation occupies the

CC BY

octahedral sites in a tetragonal spinel structure. The strong interest in this configuration arises from the unique physical and chemical properties these oxides exhibit, making them suitable for diverse applications [14,15]. $ZnMn_2O_4$ has been explored for applications such as photocatalysis [16], chemical nanosensors [17], gas sensors [18], and particularly as an anode material for lithium-ion batteries [19]. It has also shown promise in biomedicine [20], electrochemical applications [21], supercapacitors [22], negative temperature coefficient (NTC) thermistors [23], and as a precursor for the preparation of porous materials [24,25].

Photodynamic therapy (PDT) is a non-invasive treatment method that involves the administration of a photosensitizer (PS), which selectively accumulates in tumor tissues. Upon activation by light of a specific wavelength, the PS generates reactive oxygen species (ROS) in the presence of molecular oxygen, leading to cancer cell death. When irradiated, the PS transitions from its ground state to an excited singlet state ($^1PS^*$), which may return to the ground state through fluorescence or heat release. It can also undergo intersystem crossing to form a triplet state ($^3PS^*$), which can return to the ground state via phosphorescence or thermal emission. Importantly, this triplet state can engage in two types of reactions: Type I, involving electron transfer to cellular substrates to produce free radicals and subsequent oxygenated products, and Type II, involving energy transfer to molecular oxygen ($^3O_2$) to produce singlet oxygen ($^1O_2$). The resulting ROS can kill cancer cells directly through apoptosis, necrosis, or autophagy, and indirectly by damaging tumor vasculature, leading to ischemia. Additionally, PDT can stimulate an immune response against tumor-associated antigens [26-32].

In this research, $ZnMn_2O_4$ nanoparticles were synthesized using the co-precipitation method. Their structure and characteristics were confirmed using SEM, EDS, VSM, FTIR, and XRD analyses.

MATERIALS AND METHODS

Chemical reagents

Potassium manganate ($KMnO_4$), potassium hydroxide (KOH), Zinc acetate ($Zn(CH_3CO_2)_2.2H_2O$), manganese nitrate ($Mn(NO_3)_2$) and ethanol were purchased from Merck Co. All chemicals were of analytical grade and were used as received without further purification.

Synthesis of $ZnMn_2O_4$ NPs

To synthesize $ZnMn_2O_4$ nanoparticles via the co-precipitation method, Solution A was prepared by dissolving 4.5 mmol of potassium manganate ($KMnO_4$) in deionized water, followed by the dropwise addition of 25 mmol potassium hydroxide (KOH) under constant stirring. Separately, 12 mmol of zinc acetate dihydrate ($Zn(CH_3CO_2)_2{\cdot}2H_2O$) and 7.5 mmol of manganese nitrate ($Mn(NO_3)_2$) were dissolved in ethanol and deionized water, respectively, to form Solutions B and C.

Solutions B and C were then added to Solution A under continuous stirring. After 2 hours of stirring, a dark brown solution was obtained. The resulting product was washed three times with deionized water and ethanol, then separated by centrifugation at 3800 rpm for 5 minutes. The precipitate was dried in an oven at 80 °C for 4 hours, followed by calcination in a furnace at 1000 °C for 1 hour.

Material characterization

The related crystal phases and structural characterization of the synthesized sample were measured by X-ray diffraction (XRD) with using of CuK**α** with radiation (λ= 1.5406 **Å**) and RigakuD-maxcIII diffractometer. UV–visible absorption spectroscopic measurements, Photoluminescence (PL) spectrum were done by Shimadzu UV1700 spectrometer and Perkin-Elmer spectrometer model LS55 with photo multiplier tube and Xenon lamp at room temperature, Fourier transform infrared spectroscopy (FTIR) device with MagnalR550 model was used to determine the most probable functional groups by examining the frequency range of specific radiation, other devices such as: scanning electron microscope (SEM) with SEM FEI Quanta 200 model for morphology and microstructure analysis, TLD Reader Harshaw 4500 was used to heat powder samples and record their luminescence intensity in terms of time, UV–visible absorption spectroscopic Photonix Ar 2015 and Magnetic property was measured by a vibrating sample magnetometer (VSM) model AGFM/VSM 3886 from Kashan University.

RESULTS AND DISCUSSION

X-ray diffraction pattern (XRD)

X-ray diffraction (XRD) analysis was performed to identify the crystalline structure, phase composition, and degree of crystallinity of the synthesized material. This information provides

CC BY

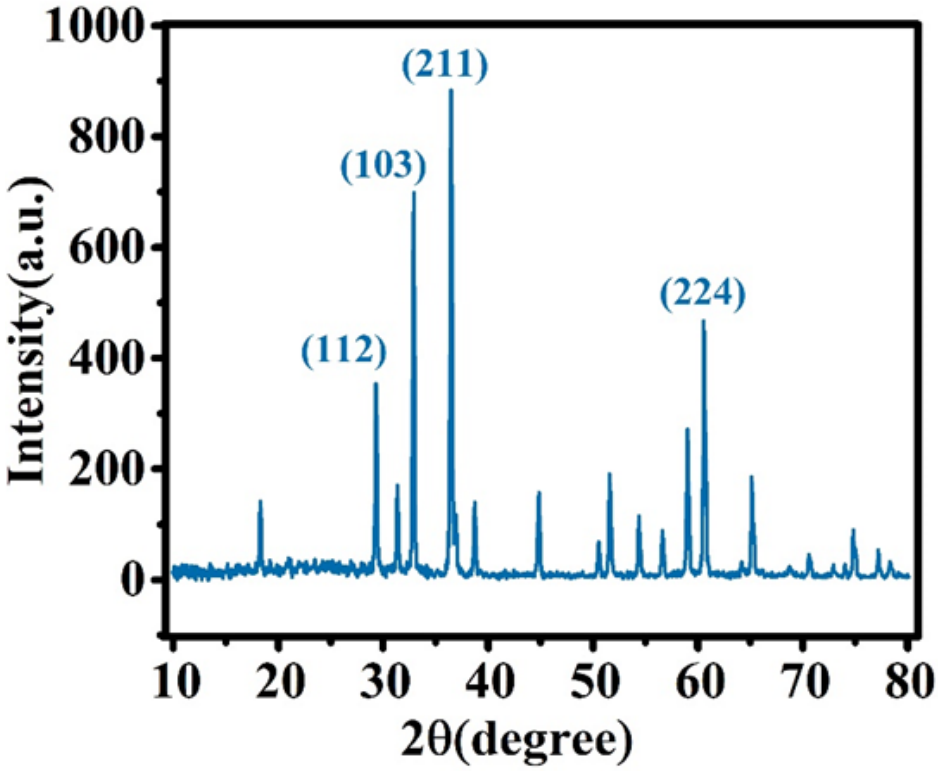

Fig. 1. XRD pattern of $ZnMn_2O_4$ Nanoparticles synthesized by co-precipitation method.

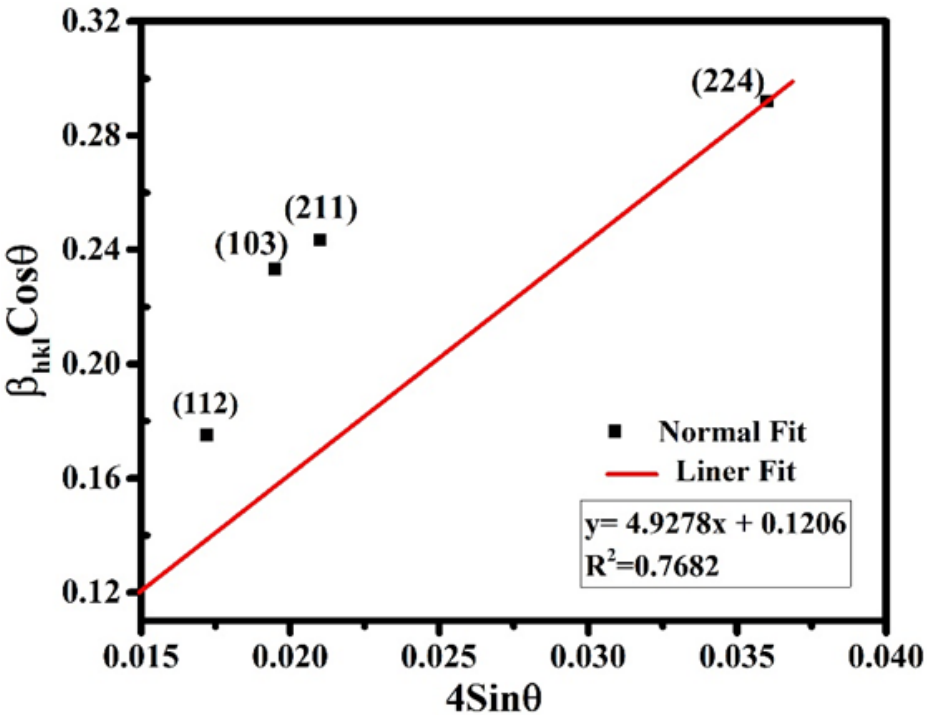

Fig. 2. UDM plot for ZnM_2nO_4 Nanoparticles.

CC BY

insights into the material's composition and microstructural features, which are critical for understanding its properties and applications. X-ray diffractograms of the as-synthesized sample powders are presented in Fig. 1. The obtained XRD pattern shows major diffraction peaks positioned at 2θ of 36.41º, 33º, 29.32º and 60.82º corresponding to the (211), (103), (112) and (224) planes, respectively. This pattern is in good agreement with the standard JCPDS No: 01-077-0470. The results indicate that the nanoparticles synthesized via the co-precipitation method have a $ZnMn_2O_4$ phase with a body-centered tetragonal structure, belonging to the space group $I4_1$ /amd. The calculated lattice constants are a= 5.720 Å, c = 9.245 Å and the unit cell volume is V= 302.32 Å. he most intense diffraction peak, corresponding to the (211) plane, was used to estimate the crystallite size using the Debye–Scherrer formula:

$$D = \frac{k\lambda}{B\cos\theta} \quad (1)$$

Where, D = crystallite size, K = Scherrer constant (usually 0.89), λ = wavelength of X-ray source (e.g., 1.5406 Å for Cu Kα radiation), β = full width at half maximum (FWHM) of the (211) plane in radians, θ = Bragg diffraction angle (in degrees).

Compared to the pristine phase, the XRD peaks of the doped material were slightly shifted to

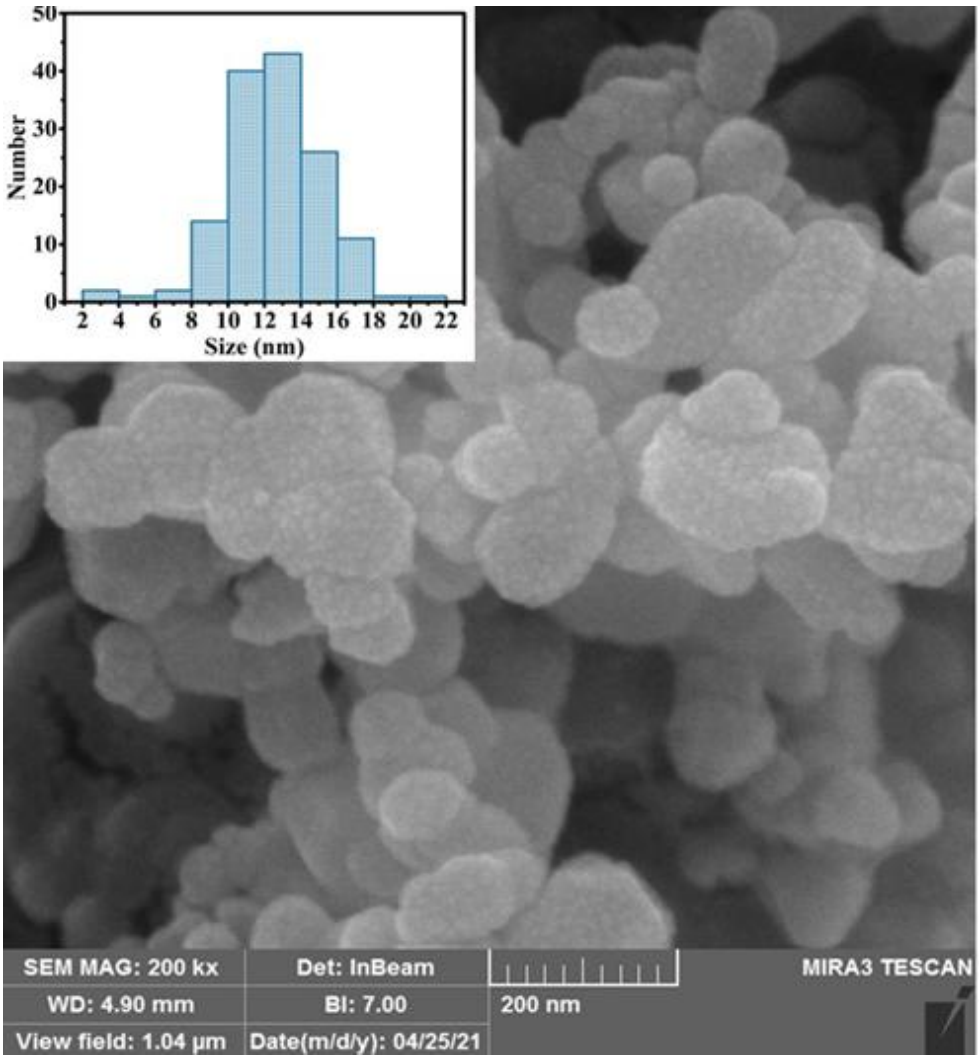

Fig. 3. SEM image of $ZnMn_2O_4$ Nanoparticles synthesized by co-precipitation method.

higher diffraction angles. This shift is attributed to the incorporation of smaller dopant ions (Zn^{2+}, Mn^{4+}) into the lattice, leading to a reduction in the lattice parameter. The degree of crystallinity was calculated based on the integrated intensities of the crystalline peaks relative to the total scattering (crystalline and amorphous regions). The material exhibited a high crystallinity index of 80%, making it suitable for structural applications. As shown in Fig. 2, $ZnMn_2O_4$ has a normal cation distribution, where Zn^{2+} ions occupy tetrahedral sites and Mn^{3+}/Mn^{4+} ions are located at octahedral sites. Neighboring Zn and Mn ions are connected through O ions. The Williamson–Hall method accounts for strain-induced XRD peak broadening and can be used to calculate both the intrinsic lattice strain and the crystallite (particle) size. $\beta_{total} = \beta_{size} + \beta_{strain}$ the total broadening due to strain and size in a particular peak having the hkl value, can be expressed as $\beta_{hkl} = \beta_{size} + \beta_{strain}$ Where, β_{hkl} is the full width at half of the maximum intensity for different diffraction planes. $\beta_{hkl} \cos\theta = k\lambda/D + 4e\sin\theta$. From the slope, the intrinsic strain was calculated to be 4.9278. The equation of the straight line is based on the Uniform Deformation Model (UDM), which assumes the isotropic nature of the crystal structure. The plotted straight line shows a good fit to the data, corresponding to all the values, as the correlation coefficient value of R^2 is 0.7682. The slope of this straight line provides the value of the intrinsic strain, whereas the intercept gives the average particle size of the $ZnMn_2O_4$ nanoparticles [33-35].

Scanning electron microscopy (SEM) image

The SEM images of $ZnMn_2O_4$ nanoparticles prepared by the co-precipitation method and calcined at 1000 °C for 1 hour are shown in Fig. 3. The high-temperature treatment resulted in notable grain size contraction and enhanced crystallinity. The samples consist entirely of agglomerated nanoparticles with a flake-like

El	Line	Atomic(% wt)	Wight(%wt)
Zn	K	6.34	13.60
Mn	K	29.23	52.62
O	K	64.43	33.78

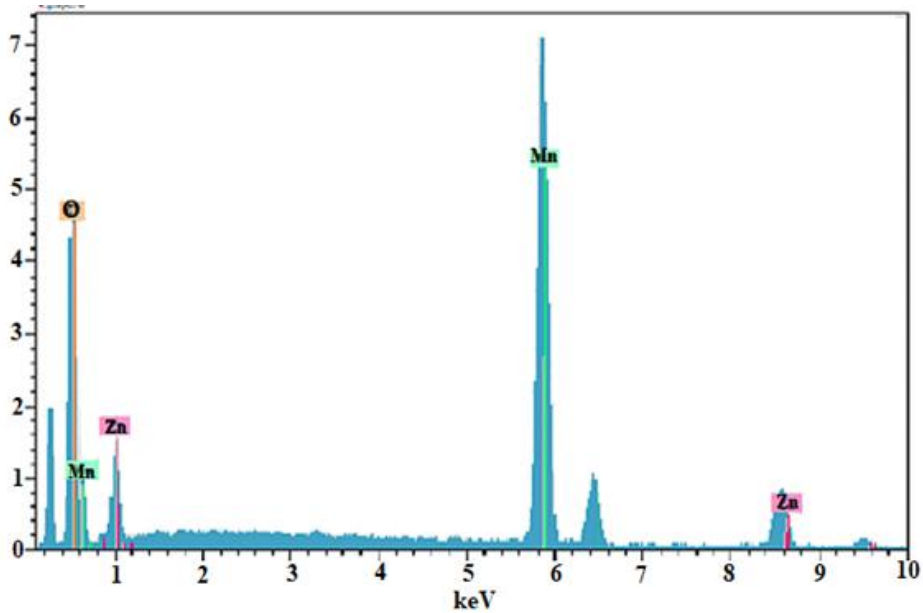

Fig. 4. EDX analysis of $ZnMn_2O_4$ Nanoparticles synthesized by co-precipitation method.

CC BY

morphology. High-magnification SEM images (scale bar: 200 nm) reveal that the flake-shaped nanoparticles possess smooth surfaces. The morphology and size of the $ZnMn_2O_4$ nanoparticles closely resemble those of their precursors, indicating that the heating process had minimal impact on particle shape. This suggests that the agglomerated Zn–Mn citrate precursor effectively serves as a structural template for producing $ZnMn_2O_4$ nanoparticles with controlled morphology. The particle size distribution ranges from 2 to 50 nm, with an average particle size of approximately 12 to 14 nm.

Energy Dispersive Analysis of X-ray

The EDX spectrum of $ZnMn_2O_4$ nanoparticles is shown in Fig. 4, confirming the presence of Zn, Mn, and O elements, indicating the successful formation of porous $ZnMn_2O_4$ microspheres. The results demonstrate that the facile co-precipitation method can produce $ZnMn_2O_4$ nanoparticles with high purity and crystallinity. The observed peaks correspond to the characteristic energies of electrons falling into the K-shell (first layer) of each element. The weight percentages of the detected elements are displayed in the figure, and no impurities were observed in the structure.

Fourier transform infrared spectrum (FTIR)

To identify and trace the functional groups of the precursor, hollow porous structure, and organic species in $ZnMn_2O_4$, the FTIR spectrum was carefully analyzed, as shown in Fig. 5. The broad band around 3441 cm^{-1} is attributed to O–H stretching vibrations, likely due to the adsorption of water molecules on the surface of the synthesized material. In the region between 700 and 400 cm^{-1}, distinct absorption peaks were observed at 641.11 cm^{-1}, 542.15 cm^{-1}, and 424.34 cm^{-1}, which are associated with M–O (M = Zn, Mn) stretching vibrations and M–O–M bending modes, respectively.

UV–visible absorption

The $ZnMn_2O_4$ exhibited an absorption band between 200 and 300 nm. The adsorption spectra

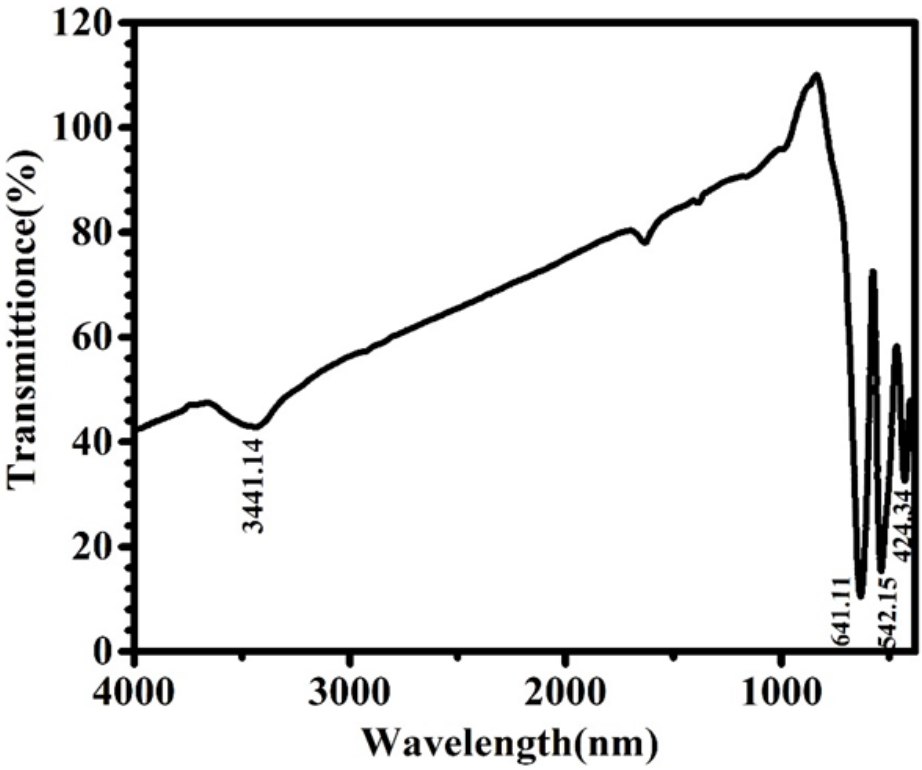

Fig. 5. FTIR of $ZnMn_2O_4$ Nanoparticles synthesized by co-precipitation method.

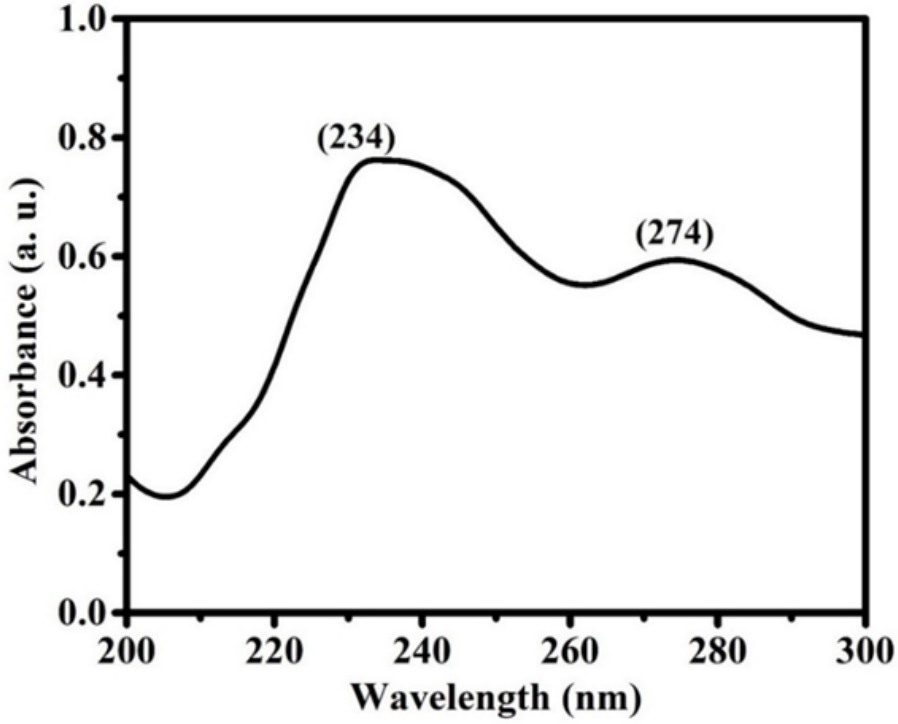

Fig. 6. UV–visible absorption and photon energy of $ZnMn_2O_4$ Nanoparticles synthesized by co-precipitation method.

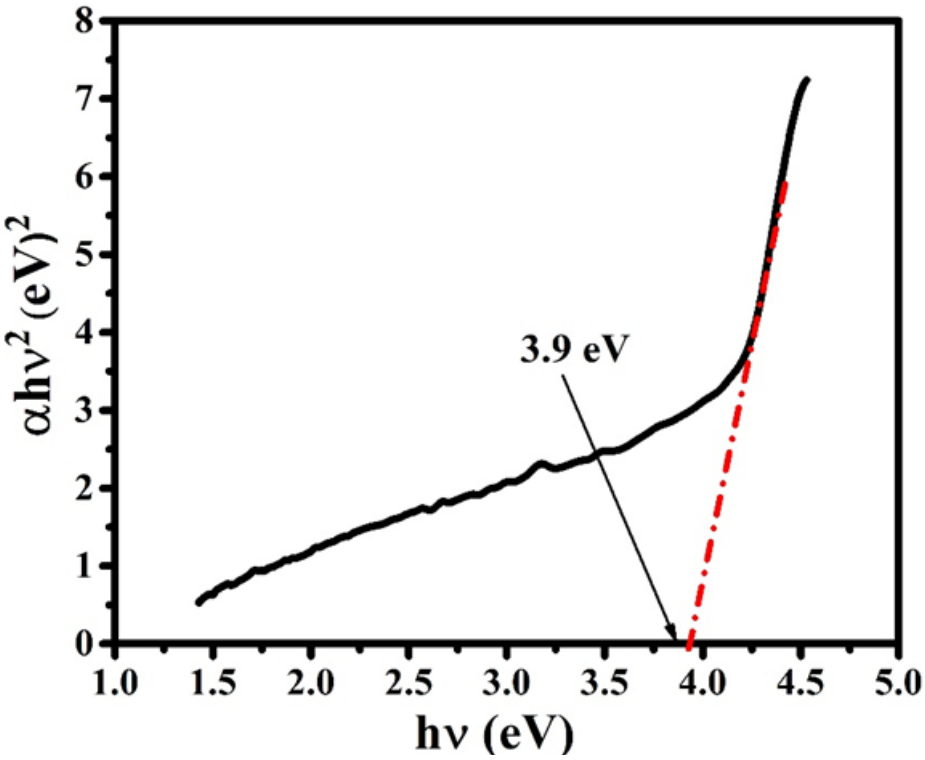

Fig. 7. Band gap of $ZnMn_2O_4$ Nanoparticles synthesized by co-precipitation method.

of $ZnMn_2O_4$ nanoparticles are visible in Fig. 6 with two peaks at 234 and 274. To calculate the band gap energy of the $ZnMn_2O_4$ nanoparticles, Tauc's formula was applied.

$$(\alpha hv)^n = B\,(hv - Eg) \quad (2)$$

E_g, **α,** hv, and B are the bandgap of the material, absorption coefficients, the energy of the incident photon, and edge width parameters independent of photon energy, respectively. The plots should be linear, with intercept equal to the interband transition energies; the exponent n equals 1/2

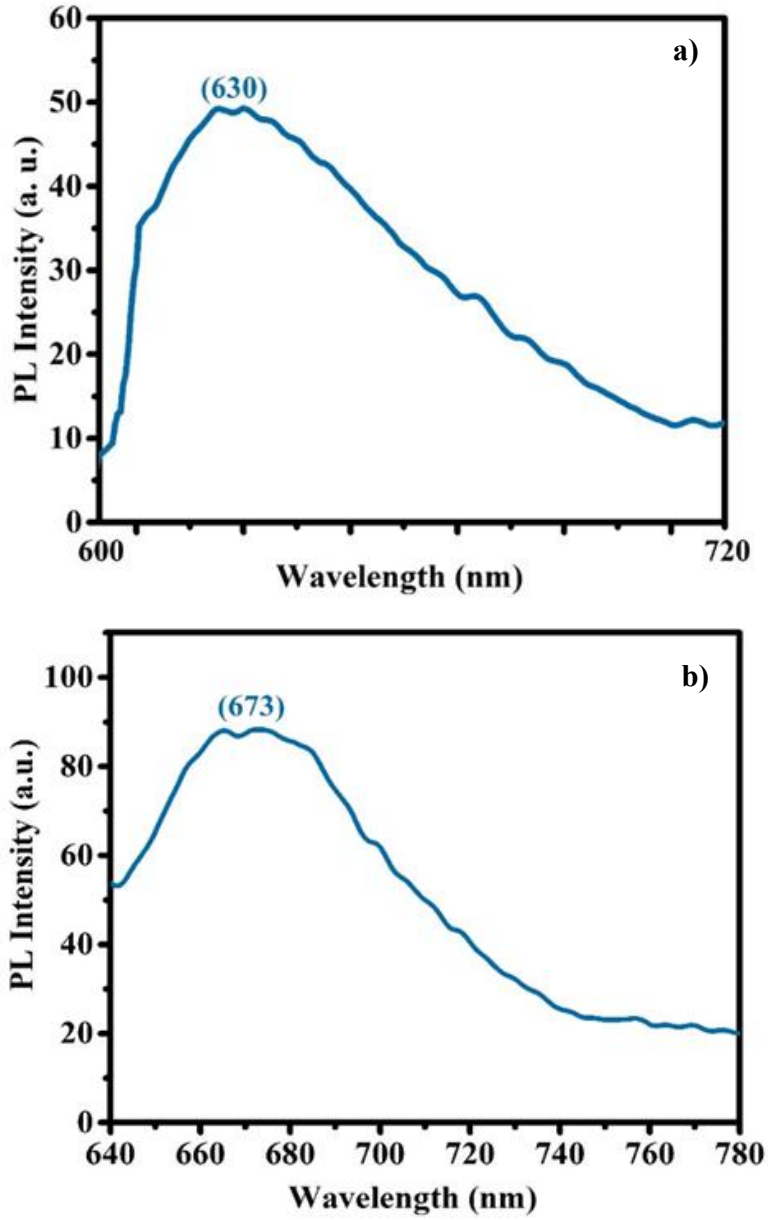

Fig. 8. a) The PL emission spectrum with the excitation wavelength of 400 nm. b) The PL emission spectrum with the excitation wavelength of 520 nm of $ZnMn_2O_4$ Nanoparticles synthesized by co-precipitation method.

for indirect allowed and 2 for direct allowed transitions. In this case, the intercept yields a band gap energy of approximately 3.9 eV [36].

Photoluminescence Spectrum

The photoluminescence (PL) spectrum of $ZnMn_2O_4$, measured at room temperature, was used to investigate its optical properties. The excitation wavelength was set at 400 nm, and the resulting emission spectrum exhibited a peak at 630 nm in the infrared region. Additionally, when the excitation wavelength was increased to 520 nm, as shown in Fig. 8, a redshift in the emission peak was observed—from 630 nm to 673 nm—indicating that reducing the excitation energy leads to an increase in the emission wavelength. This redshift can be attributed to the quantum confinement effect and the variation in particle size distribution. The observed emission is likely due to electron transitions between the defect states and the conduction or valence bands, which are commonly present in transition metal oxides. The presence of manganese and zinc ions in different oxidation states can also introduce localized energy levels within the bandgap, contributing to the observed PL response. Such tunable luminescent properties make $ZnMn_2O_4$ nanoparticles promising candidates for optoelectronic devices, biological imaging, and sensor applications. Furthermore, the high crystallinity and purity of the synthesized nanoparticles enhance their emission intensity, confirming the structural integrity of the material.

The luminescence intensity in terms of time

The afterglow emission of $ZnMn_2O_4$ nanoparticles can be detected even after 20 minutes of UVA irradiation. This observation is consistent with the data shown in the inset of Fig. 9, where measurable emission is still detected 200 seconds after the cessation of UVA exposure. Notably, the afterglow intensity increased by approximately 0.5× nm. The area under the emission curve corresponds to the amount of charge stored by the nanoparticles, calculated to be around 300.9 nC. These findings indicate that $ZnMn_2O_4$ nanoparticles possess self-irradiating properties, enabling them to continue emitting light after the excitation source is removed.

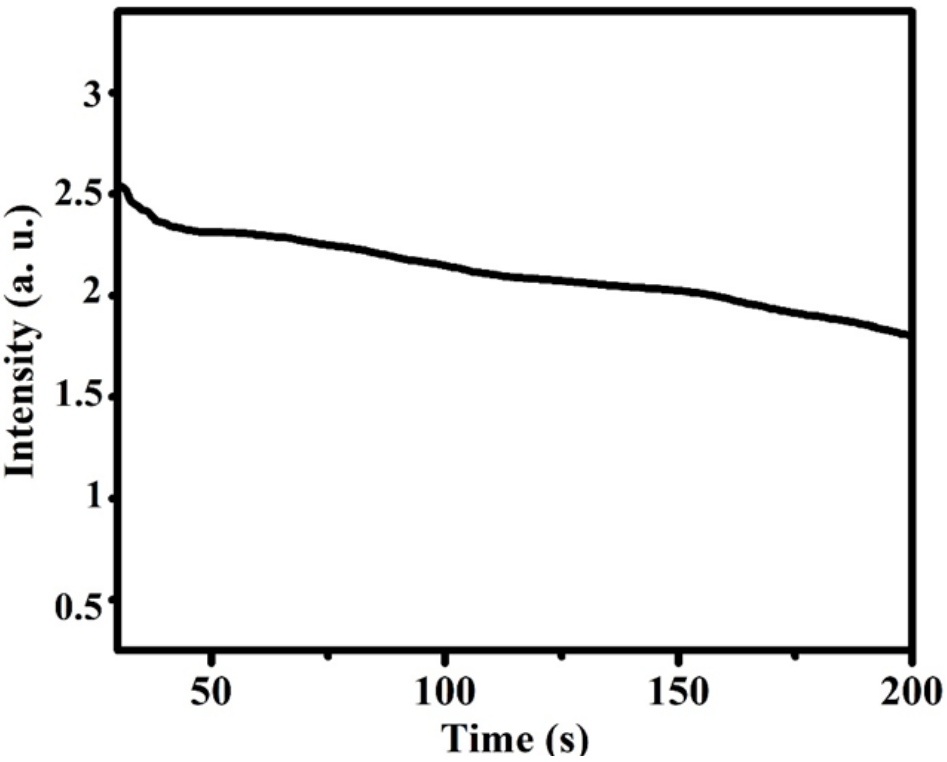

Fig. 9. The afterglow spectrum of $ZnMn_2O_4$ Nanoparticles synthesized by co-precipitation method.

CC BY

This persistent luminescence behavior makes them promising candidates for applications in bioimaging, optical storage, and security tagging.

ROS measurement

In this study, the levels of Reactive Oxygen Species (ROS) were measured using Anthracene and Methylene blue reagents. The production of singlet oxygen and hydroxyl radicals can be identified by the reduction in the absorption or emission intensity of anthracene and methylene blue reagents, respectively, following their reaction with these reactive oxygen species. Due to their specific trapping by anthracene and methylene blue respectively. The decreasing absorption intensity of these trapped materials

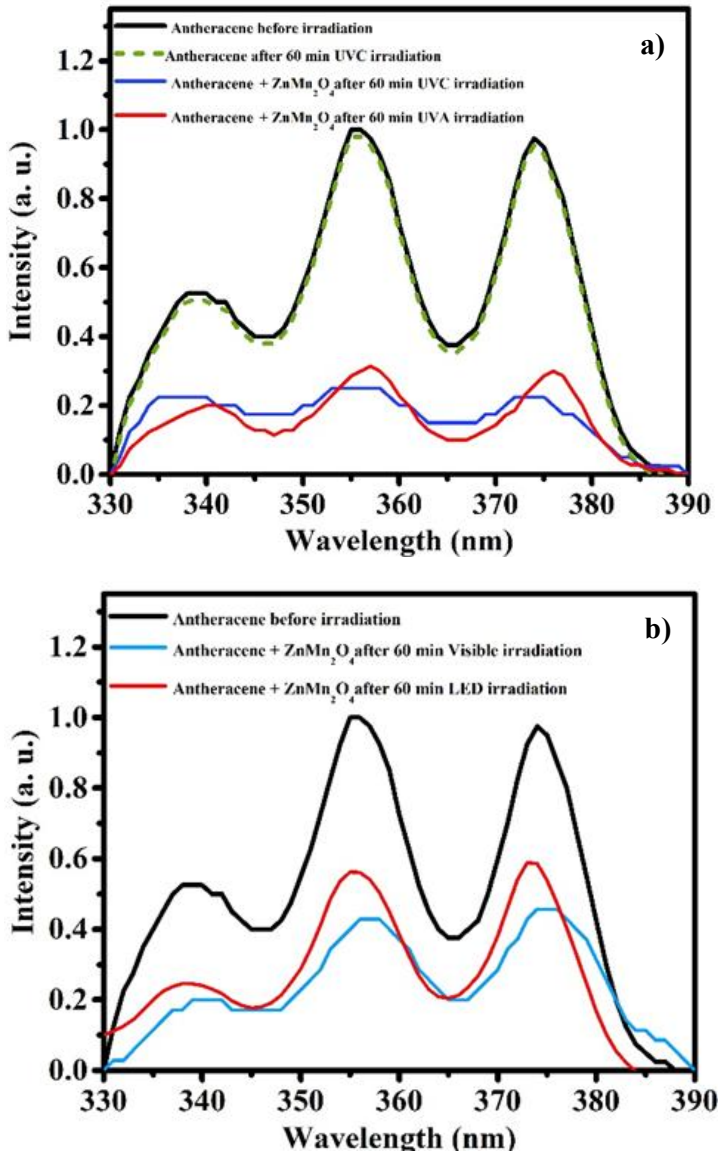

Fig. 10. (a) Reduction of anthracene absorbance intensity before and after 60 min UVC and UVA irradiation (b) Reduction of anthracene absorbance intensity before and after 60 min Visible and LED power (and for better comparison all the graphs normaled to 1).

represents ROS production. Fig. 10 shows a decrease in anthracene absorbance intensity after 60 minutes of irradiation with UVC, UVA, visible light (simulator lamp), and LED power light. To observe the decrease in anthracene absorbance intensity caused by these nanoparticles at longer wavelengths, visible and LED power light in yellow, green, and indigo colors—with wavelengths of 480, 520, and 580 nm—were used for 60 minutes. This decrease indicates the generation of singlet oxygen ($^1O_2$). The decrease in anthracene absorbance intensity after 60 minutes of UVC, UVA, visible (simulator lamp), and LED power light irradiation was found to be 83%, 85%, 64%, and 55%, respectively. Fig. 11 shows the decrease in methylene blue absorbance intensity before and after 60 minutes of irradiation under the same light sources, which indicates the generation of hydroxyl radicals (•OH). The reduction percentages in methylene blue absorbance were 23% for UVC, 50% for UVA, 82% for visible light, and 20% for LED light. These results confirm that the synthesized $ZnMn_2O_4$ nanoparticles, without any impurities or external photosensitizers, are capable of generating reactive oxygen species (ROS), effectively acting as intrinsic photosensitizers (PS). This study underscores the critical role of ROS in photodynamic therapy (PDT), and highlights how understanding the mechanisms and efficiency of ROS generation can inform the design of more effective nanomaterials for cancer treatment.

VSM analysis

The most commonly employed technique for magnetic measurements is the Vibrating Sample Magnetometer (VSM). Fig. 12 illustrates the magnetization (M) versus magnetic field (H) curve for $ZnMn_2O_4$ nanoparticles synthesized at 1000 °C. The hysteresis loop reveals a remanent magnetization (Mr) of 0.024 emu/g, a coercive field (Hc) of 145 Oe, and a saturation magnetization (Ms) of 0.9597 emu/g. These results indicate that the nanoparticles exhibit weak antiferromagnetic behavior and possess

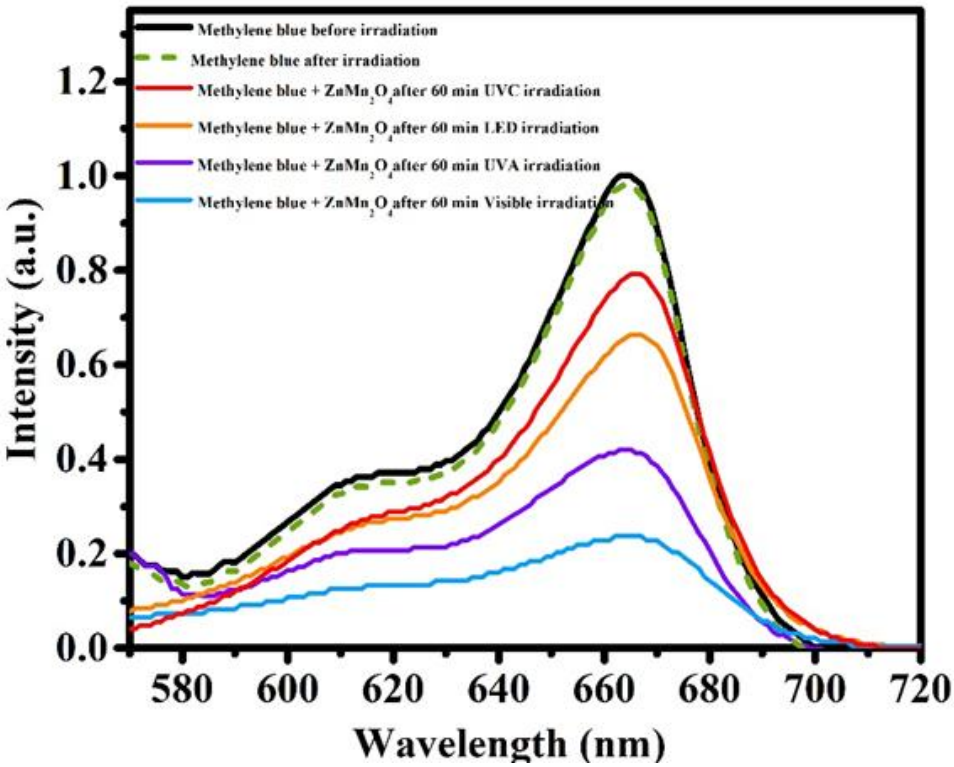

Fig. 11. Reduction of methylene blue absorbance intensity with different source lights, (LED power < UVC < UVA< Visible).

CC BY

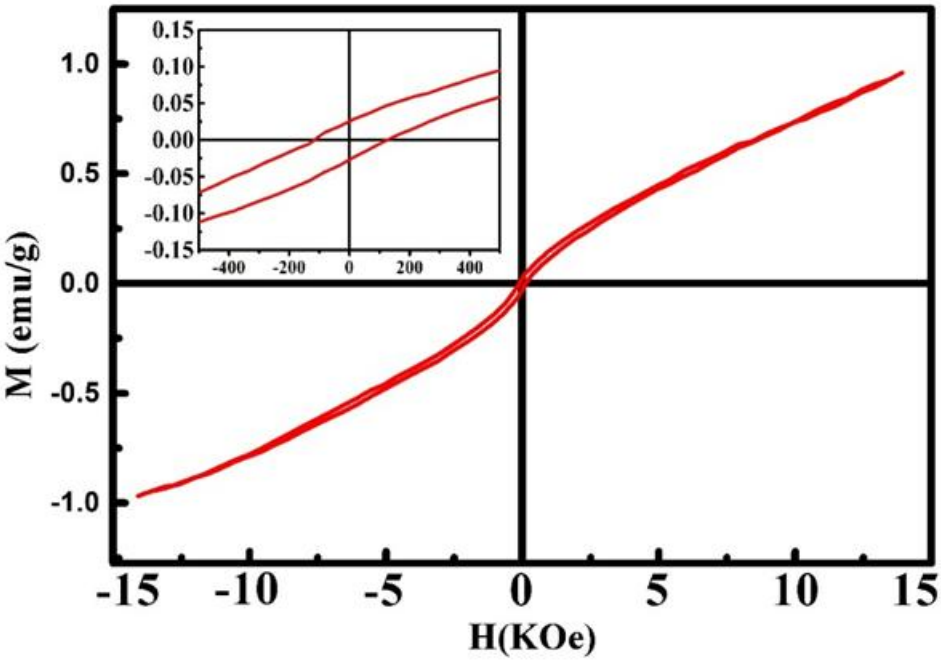

Fig. 12. The VSM analyze of $ZnMn_2O_4$ Nanoparticles synthesized by co-precipitation method.

soft magnetic properties. Such soft magnetic characteristics are advantageous for applications involving magnetic guidance, such as targeted drug delivery using magnetic nanoparticles.

CONCLUSION

$ZnMn_2O_4$ nanoparticles (NPs) were synthesized via the co-precipitation method. Their nanostructural, optical, and magnetic properties were thoroughly characterized using XRD, FESEM, EDS, FTIR, UV-Vis's absorption spectroscopy, photoluminescence (PL), and VSM analysis. The PL emission spectra of the synthesized nanoparticles exhibited broad peaks at 630 nm and 673 nm under different excitation wavelengths. The reduction in anthracene absorbance intensity upon exposure to UVC, UVA, and visible light in the presence of the nanoparticles confirms the generation of singlet oxygen (^1O_2). Additionally, methylene blue absorbance decreased by up to 82% after 60 minutes of visible light irradiation, indicating hydroxyl radical (•OH) generation. These results demonstrate that the $ZnMn_2O_4$ nanoparticles not only possess ferromagnetic properties, making them suitable for magnetically guided drug delivery, but also exhibit excellent capability for reactive oxygen species (ROS) generation, highlighting their potential as photosensitizers in photodynamic therapy (PDT).

ACKNOWLEDGMENTS

The authors gratefully acknowledge the research council of the University of Kashan for financial support of this research, etc.

CONFLICT OF INTEREST

The authors declare that there is no conflict of interests regarding the publication of this manuscript.

REFERENCES

1. Zhao J, Duan L, Wang A, Fei J, Li J. Insight into the efficiency of oxygen introduced photodynamic therapy (PDT) and deep PDT against cancers with various assembled nanocarriers. WIREs Nanomedicine and Nanobiotechnology. 2019;12(1).
2. Wang Y, Gong N, Li Y, Lu Q, Wang X, Li J. Atomic-Level Nanorings (A-NRs) Therapeutic Agent for Photoacoustic Imaging and Photothermal/Photodynamic Therapy of Cancer. Journal of the American Chemical Society. 2019;142(4):1735-1739.
3. Azizi A, Shademan S, Rezai M, Rahimi A, Lawaf S. Effect of photodynamic therapy with two photosensitizers on Streptococcus mutants: In vitro study. Photodiagnosis Photodyn Ther. 2016;16:66-71.
4. Wang W-E, Chang C-H. Successful treatment of extremely large Bowen's disease lesion by topical photodynamic therapy and imiquimod: Using optical coherence tomography to detect

early recurrence loci and validate the cure. Photodiagnosis Photodyn Ther. 2023;41:103201.
5. Nguyen LNM, Lin ZP, Sindhwani S, MacMillan P, Mladjenovic SM, Stordy B, et al. The exit of nanoparticles from solid tumours. Nature Materials. 2023;22(10):1261-1272.
6. Chen J, Fan T, Xie Z, Zeng Q, Xue P, Zheng T, et al. Advances in nanomaterials for photodynamic therapy applications: Status and challenges. Biomaterials. 2020;237:119827.
7. Sai DL, Lee J, Nguyen DL, Kim Y-P. Tailoring photosensitive ROS for advanced photodynamic therapy. Experimental and Molecular Medicine. 2021;53(4):495-504.
8. Kirar S, Chaudhari D, Thakur NS, Jain S, Bhaumik J, Laha JK, et al. Light-assisted anticancer photodynamic therapy using porphyrin-doped nanoencapsulates. J Photochem Photobiol B: Biol. 2021;220:112209.
9. Liu J, Yao Z, Qiu G, Wan Y, Song W, Zeng H, et al. Generation of reactive oxygen species through dissolved oxygen activation on defected porous carbon for efficient degradation of antibiotics. Chem Eng J. 2023;455:140602.
10. Glorieux C, Liu S, Trachootham D, Huang P. Targeting ROS in cancer: rationale and strategies. Nature Reviews Drug Discovery. 2024;23(8):583-606.
11. Wang J, Qu C, Shao X, Song G, Sun J, Shi D, et al. Carrier-free nanoprodrug for p53-mutated tumor therapy via concurrent delivery of zinc-manganese dual ions and ROS. Bioactive Materials. 2023;20:404-417.
12. Naser SS, Ghosh B, Simnani FZ, Singh D, Choudhury A, Nandi A, et al. Emerging Trends in the Application of Green Synthesized Biocompatible ZnO Nanoparticles for Translational Paradigm in Cancer Therapy. Journal of Nanotheranostics. 2023;4(3):248-279.
13. Wang Y, Gao F, Zhao L, Wu Y, Li C, Li H, et al. Enhancing cancer treatment via "Zn^{2+} interference" with Zn-based nanomaterials. Coord Chem Rev. 2024;500:215535.
14. Aruchamy K, Nagaraj R, Manohara HM, Nidhi MR, Mondal D, Ghosh D, et al. One-step green route synthesis of spinel $ZnMn_2O_4$ nanoparticles decorated on MWCNTs as a novel electrode material for supercapacitor. Materials Science and Engineering: B. 2020;252:114481.
15. Zhandun VS, Nemtsev AV. Ab initio comparative study of the magnetic, electronic and optical properties of AB_2O_4 (A, B= Mn, Fe) spinels. Materials Chemistry and Physics. 2021;259:124065.
16. Zhao L, Li X, Zhao J. Fabrication, characterization and photocatalytic activity of cubic-like $ZnMn_2O_4$. Appl Surf Sci. 2013;268:274-277.
17. Nassar MY, El-Moety EA, El-Shahat MF. Synthesis and characterization of a $ZnMn_2O_4$ nanostructure as a chemical nanosensor: a facile and new approach for colorimetric determination of omeprazole and lansoprazole drugs. RSC Advances. 2017;7(69):43798-43811.
18. Morán-Lázaro J, Guillen-López E, López-Urias F, Muñoz-Sandoval E, Blanco-Alonso O, Guillén-Bonilla H, et al. Synthesis of $ZnMn_2O_4$ Nanoparticles by a Microwave-Assisted Colloidal Method and their Evaluation as a Gas Sensor of Propane and Carbon Monoxide. Sensors. 2018;18(3):701.
19. Bai Z, Fan N, Sun C, Ju Z, Guo C, Yang J, et al. Facile synthesis of loaf-like $ZnMn_2O_4$ nanorods and their excellent performance in Li-ion batteries. Nanoscale. 2013;5(6):2442.
20. Zou J, Liu B, Liu H, Ding Y, Xin T, Wang Y. Facile synthesis of interconnected mesoporous $ZnMn_2O_4$ nano-peanuts for Li-storage via distinct structure design. Mater Res Bull. 2018;107:468-476.
21. Biotemplate-Based Engineering of High-Temperature Stable Anatase TiO_2 Nanofiber Bundles with Impregnated CeO_2 Nanocrystals for Enhanced Lithium Storage. American Chemical Society (ACS).
22. Guillemet-Fritsch S. Structure, thermal stability and electrical properties of zinc manganites. Solid State Ionics. 2000;128(1-4):233-242.
23. Toberer ES, Seshadri R. Spontaneous Formation of Macroporous Monoliths of Mesoporous Manganese Oxide Crystals. Adv Mater. 2005;17(18):2244-2246.
24. Kim Y, Uthaman S, Pillarisetti S, Noh K, Huh KM, Park I-K. Bioactivatable reactive oxygen species-sensitive nanoparticulate system for chemo-photodynamic therapy. Acta Biomater. 2020;108:273-284.
25. Bayati-Komitaki N, Ganduh SH, Alzaidy AH, Salavati-Niasari M. A comprehensive review of Co3O4 nanostructures in cancer: Synthesis, characterization, reactive oxygen species mechanisms, and therapeutic applications. Biomedicine and Pharmacotherapy. 2024;180:117457.
26. Dąbrowski JM. Reactive Oxygen Species in Photodynamic Therapy: Mechanisms of Their Generation and Potentiation. Advances in Inorganic Chemistry: Elsevier; 2017. p. 343-394.
27. Kwiatkowski S, Knap B, Przystupski D, Saczko J, Kędzierska E, Knap-Czop K, et al. Photodynamic therapy – mechanisms, photosensitizers and combinations. Biomedicine and Pharmacotherapy. 2018;106:1098-1107.
28. Dos Santos AlF, De Almeida DRQ, Terra LF, Baptista McS, Labriola L. Photodynamic therapy in cancer treatment - an update review. Journal of Cancer Metastasis and Treatment. 2019;2019.
29. Nurtdinova L, Semashko V, Guyot Y, Korableva S, Joubert MF, Nizamutdinov A. Application of photoconductivity measurements to photodynamic processes investigation in LiYF4:Ce3+ and LiLuF4:Ce3+ crystals. Opt Mater. 2011;33(10):1530-1534.
30. Lin X, Li W, Wen Y, Su L, Zhang X. Aggregation-induced emission (AIE)-Based nanocomposites for intracellular biological process monitoring and photodynamic therapy. Biomaterials. 2022;287:121603.
31. Sarikaya SY, Alidagi HA, Cetindere S. Novel BODIPY-Fluorene-Fullerene and BODIPY-Fluorene-BODIPY Conjugates: Synthesis, Characterization, Photophysical and Photochemical Properties. Journal of Fluorescence. 2022;33(1):297-304.
32. Zhang Y, Tian S, Huang L, Li Y, Lu Y, Li H, et al. Reactive oxygen species-responsive and Raman-traceable hydrogel combining photodynamic and immune therapy for postsurgical cancer treatment. Nature Communications. 2022;13(1).
33. Gelfond M, Kondratiev S, Tkachenko E, Semiglazov V, Semiglazova T, Ivanov V, et al. Photodynamic therapy in the combined treatment of breast cancer intradermal metastases. 2020 International Conference Laser Optics (ICLO); 2020/11/02: IEEE; 2020. p. 1-1.
34. Magalhães S, Cabaço JS, Mateus R, Faye DN, Pereira DR, Peres M, et al. Crystal mosaicity determined by a novel layer deconvolution Williamson–Hall method. CrystEngComm. 2021;23(10):2048-2062.
35. Choudhury RR, Chitra R, Ramanadham M. Investigation of diffraction line broadening due to compositional fluctuations in L-alanine-doped triglycine sulfate. Acta Crystallographica Section B Structural Science. 2003;59(5):647-652.
36. Wood DL, Tauc J. Weak Absorption Tails in Amorphous Semiconductors. Physical Review B. 1972;5(8):3144-3151.

CC BY